

# Path-integral Monte Carlo simulations of solid parahydrogen using two-body, three-body, and four-body *ab initio* interaction potential energy surfaces

Alexander Ibrahim<sup>1,2</sup> and Pierre-Nicholas Roy<sup>2, a)</sup>

<sup>1)</sup>Department of Physics and Astronomy, University of Waterloo, 200 University Avenue West, Waterloo, Ontario N2L 3G1, Canada

<sup>2)</sup>Department of Chemistry, University of Waterloo, 200 University Avenue West, Waterloo, Ontario N2L 3G1, Canada

We present path integral Monte Carlo simulation results for the equation of state of solid parahydrogen between  $0.024 \text{ \AA}^{-3}$  and  $0.1 \text{ \AA}^{-3}$  at  $T = 4.2 \text{ K}$ . The simulations are performed using non-additive isotropic *ab initio* two-body, three-body, and four-body potential energy surfaces (PES). We apply corrections to account for both the finite size simulation errors and the Trotter factorization errors. Simulations that use only the two-body PES during sampling yield an equation of state similar to that of simulations that use both the two-body and three-body PESs during sampling. With the four-body interaction energy, we predict an equilibrium density of  $0.02608 \text{ \AA}^{-3}$ , very close to the experimental result of  $0.0261 \text{ \AA}^{-3}$ . The inclusion of the four-body interaction energy also brings the simulation results in excellent agreement with the experimental pressure-density data until around  $0.065 \text{ \AA}^{-3}$ , beyond which the simulation results overestimate the pressure. These PESs overestimate the average kinetic energy per molecule at the equilibrium density by about 7% compared to the experimental result. Our findings suggest that, at higher densities, we require five-body and higher-order many-body interactions to quantitatively improve the agreement between the pressure-density curve produced by simulations, and that of experiment. Using the four-body PES during sampling at excessively high densities, where such higher-order many-body interactions are likely to be significant, causes an artificial symmetry breaking in the *hcp* lattice structure of the solid.

## I. INTRODUCTION

Solid parahydrogen (*para*-H<sub>2</sub>) is a quantum molecular solid that displays a wide variety of exotic quantum behaviours.<sup>1–4</sup> The most striking of these behaviours is its abnormally large zero-point kinetic energy, which is due to the low mass of, and weak intermolecular interactions between, the *para*-H<sub>2</sub> molecules.<sup>3,5,6</sup> Each *para*-H<sub>2</sub> molecule has a very large translational displacement about its nominal lattice site. For example, at the solid's equilibrium density of  $\rho_0 = 0.0261 \text{ \AA}^{-3}$ <sup>7,8</sup> the ratio of the root mean square displacement of each *para*-H<sub>2</sub> molecule from its nominal lattice site to the lattice constant is about 20%.<sup>7–9</sup> Solid *para*-H<sub>2</sub> can be visualized as an *hcp* lattice with a nearly spherically symmetric decaying probability cloud for each *para*-H<sub>2</sub> molecule centred at each lattice site.

Most simulations of solid parahydrogen are done using pointwise pair potentials.<sup>10–16</sup> All pair potentials between hydrogen molecules share several common features. Each one has a strong repulsive wall at short pair distances, a deep attractive well around  $3 \text{ \AA}$ , and a weak decaying attractive tail to model the dispersion interaction. Pointwise pair potentials are very common because they are computationally efficient, easy to implement, and provide accurate results under certain conditions. However, it has become increasingly apparent that we cannot accurately model solid *para*-H<sub>2</sub> using only pair potentials, especially at high densities.<sup>17,18</sup> A complete model of solid *para*-H<sub>2</sub> requires the use of many-body interactions.

Non-additive many-body interactions, such as the three-body and four-body interaction, are very weak compared to the two-body interaction except at very short intermolecular distances.<sup>19,20</sup> In many chemical systems, many-body interactions are either completely negligible or can be treated as a slight perturbation to the dominant two-body interaction. However, the large translational displacement of each *para*-H<sub>2</sub> molecule about its nominal lattice site causes its probability distribution to spill into very short intermolecular spacings. As a result, solid *para*-H<sub>2</sub> is very sensitive to the effects of non-additive many-body interaction potentials.

Several computational studies have emphasized the importance of the three-body interaction potential for *para*-H<sub>2</sub>.<sup>21–25</sup> The importance of many-body interaction potentials has also been demonstrated in other systems, such as bulk systems of helium<sup>26–31</sup> solid neon,<sup>26,32</sup> solid and gaseous argon,<sup>26,33,34</sup> and solid krypton.<sup>35</sup> In a recent simulation study, Wheatley *et al.* created an *ab initio* four-body potential energy surface (PES) for helium and investigated its importance in predicting the fourth virial coefficient of helium.<sup>36</sup> In another recent work, Morresi and Garberoglio used the aforementioned four-body PES for helium to perform PIMC simulations of superfluid and normal liquid helium-4.<sup>37</sup>

Advancements in both quantum chemistry and machine learning have made it possible to create PESs for *ab initio* many-body systems.<sup>38–40</sup> We collect the *ab initio* training data energies by directly solving the time-independent Schrödinger equation on a computer, and then use a machine learning method to create a PES that maps the relevant coordinates to their corresponding interaction energies.<sup>41</sup> Unlike phenomenological PESs, *ab*

<sup>a)</sup>Electronic mail: pnroy@uwaterloo.ca

*ab initio* PESs have no dependence on the results of any specific experiment, and can be constructed to contain the different many-body contributions explicitly.

In this work, we calculate the equation of state (EOS) of solid parahydrogen at  $T = 4.2\text{ K}$  using path-integral Monte Carlo (PIMC) simulations. The solid is modelled as a hexagonal close-packed (*hcp*) lattice between the densities of  $0.024\text{ \AA}^{-3}$  and  $0.1\text{ \AA}^{-3}$ . The simulations are performed using non-additive *ab initio* two-body, three-body, and four-body PESs for *para*-H<sub>2</sub> previously published by this research group.<sup>16,42,43</sup> We show how the inclusion or omission of the different PESs during the sampling and estimation phases of the PIMC simulation affect the energy-density relationship, the pressure-density relationship, and the position distribution of molecules in the solid. We also show how the separate energy components (kinetic, two-body potential, three-body potential, and four-body potential) change as a function of density.

The remainder of this paper is structured as follows: In Sec. (II), we present the model of the solid, including the Hamiltonian that describes it, a description of the three *ab initio* PESs used in the simulations, and the sampling strategies used in the work. In Sec. (III), we briefly discuss the PIMC simulation technique, and how we correct the systemic Trotter and finite system size errors inherent to performing PIMC simulations of solids. In Sec. (IV), we present and discuss the findings of our work. Finally, in Sec. (V), we present both our conclusions as well as suggestions for future work.

## II. MODEL

### A. Hamiltonian

We model the solid as a collection of  $N = 180$  pointwise *para*-H<sub>2</sub> molecules in three spatial dimensions. The molecules are placed at *hcp* lattice sites within a rectangular prism, with periodic boundary conditions applied in all three dimensions. The Hamiltonian for the system is

$$\hat{H} = -\frac{\hbar^2}{2m} \sum_{i=1}^N \nabla_i^2 + \sum_{i < j}^N \hat{V}_2(r_{ij}) + \sum_{i < j < k}^N \hat{V}_3(r_{ij}, r_{ik}, r_{jk}) + \sum_{i < j < k < l}^N \hat{V}_4(r_{ij}, r_{ik}, r_{il}, r_{jk}, r_{jl}, r_{kl}) \quad (1)$$

where  $m$  is the mass of each *para*-H<sub>2</sub> molecule,  $r_{ij}$  is the relative distance between the centres of mass of molecules with labels  $i$  and  $j$ , and  $\hat{V}_2$ ,  $\hat{V}_3$  and  $\hat{V}_4$  are the two-body, three-body, and four-body PESs, respectively.<sup>16,42,43</sup>

We model the *para*-H<sub>2</sub> molecules as pointwise particles interacting with one another through isotropic potentials. The two-body PES implicitly accounts for rota-

tional and vibrational degrees of freedom in an adiabatic manner, while the three-body and four-body PESs omit them entirely. This is a reasonable assumption to make while in phase I of the  $P$ - $T$  phase region of H<sub>2</sub>, which, at  $T = 4.2\text{ K}$ , extends from  $P = 0\text{ GPa}$  up to around  $P = 60\text{ GPa}$ .<sup>44</sup> Even at the highest densities explored in this work, our simulations do not exceed pressures of  $22\text{ GPa}$ . In phases at higher pressures, rotational degrees of freedom beyond the adiabatic hindered rotor component become more important,<sup>45,46</sup> and the vibrationally averaged bond length decreases.<sup>47</sup> As a result, we would need PESs with explicit rotational and vibrational degrees of freedom to accurately simulate solid *para*-H<sub>2</sub> to even higher pressures.

### B. Potential Energy Surfaces

The PIMC simulations in this work are performed with three different *ab initio* PESs for *para*-H<sub>2</sub>. The energies used in the training data for each of these PESs were collected from electronic structure calculations. All the energies were calculated at the correlated coupled-cluster theory level, with singles, doubles, and perturbative triples excitations (CCSD(T)). The calculations were performed using augmented correlation-consistent polarized valence zeta basis sets of cardinality  $N$  (AVNZ), where  $N = \{D, T, Q, \dots\}$ . Each calculation is supplemented by a (3s3p2d) midbond basis at the centre of mass of the atoms.

For the two-body interaction, we use the Faruk-Schmidt-Hinde (FSH) potential. This PES was created in 2014,<sup>16,48</sup> when Faruk *et al.* applied the adiabatic hindered rotor method<sup>49–53</sup> to a full six-dimensional H<sub>2</sub>–H<sub>2</sub> PES published by Hinde.<sup>14</sup> This is an adiabatic treatment in which the centre of mass pair distance is treated as the “slow” coordinate, while the remaining vibrational and rotational degrees of freedom are treated as the “fast” coordinates. The result is an isotropic 1D PES which treats the two *para*-H<sub>2</sub> molecules in a pointwise manner, and whose only parameter is the centre of mass distance between the two molecules. In previous studies, the FSH potential has successfully predicted the experimentally observed first vibrational shifts of small *para*-H<sub>2</sub> molecule clusters.<sup>16,48,54,55</sup> The energies used in the original 6D H<sub>2</sub>–H<sub>2</sub> PES by Hinde were calculated at the CCSD(T) level, using AVQZ atom-centred basis sets.<sup>14</sup> The two-body PES is implemented in the simulation using 1D linear interpolation.

For the three-body interaction, we use a non-additive *ab initio* three-body *para*-H<sub>2</sub> interaction PES published by this research group in 2022.<sup>42</sup> The energies used in the training data were calculated at the CCSD(T) level, using AVTZ atom-centred basis sets, with the MRCC program (version 2019).<sup>56,57</sup> The energies are isotropic, and the PES is a function of only the three centre of mass pair distances between the three *para*-H<sub>2</sub> molecules. The rigid rotor approximation removes the three bond length

degrees of freedom, and the six-point Lebedev quadrature scheme is used to spherically average over the six rotational degrees of freedom. The published three-body PES uses a reproducing-kernel Hilbert space (RKHS) toolkit to interpolate the training data.<sup>58</sup> For this work, we change the implementation for the three-body PES from the RKHS method to trilinear interpolation. The training data for the new PES is collected by evaluating the original PES in a fine grid of Jacobi coordinates. This change in implementation drastically improves the evaluation time of the three-body interaction, at the expense of increasing the required amount of memory. Evaluating both three-body PESs on PIMC simulation snapshots from three different densities ( $\rho = 0.024 \text{ \AA}^{-3}$ ,  $0.062 \text{ \AA}^{-3}$ ,  $0.1 \text{ \AA}^{-3}$ ) shows that the estimates of the average three-body potential energy per molecule between the two implementations are within  $0.003 \text{ cm}^{-1}$ ,  $0.01 \text{ cm}^{-1}$ , and  $0.08 \text{ cm}^{-1}$ , respectively. The fit error is still much smaller than the systemic finite basis set size error from using the AVTZ basis set.<sup>42</sup>

For the four-body interaction, we use an *ab initio* four-body *para*-H<sub>2</sub> interaction PES recently published by this research group.<sup>43</sup> The energies in the training data were calculated at the CCSD(T) level, using AVDZ atom-centred basis sets, with the MRCC program (version 2019).<sup>56,57</sup> As is the case for the three-body PES, the energies in the four-body PES are isotropic, being a function of only the six centre of mass pair distances between the four *para*-H<sub>2</sub> molecules. We use the rigid rotor approximation and the six-point Lebedev quadrature scheme to remove the vibrational and rotational degrees of freedom. The four-body PES is implemented using a feed-forward neural network in C++ libtorch.<sup>38</sup>

There are certain regions of coordinate space for which the accuracy of the aforementioned PESs are unknown or limited. However, for the range of conditions explored in these simulations, the effect of these limitations on the results is minimal. For example, all three PESs were built using *ab initio* training data with side lengths greater than 2.2 Å, and each of them relies on exponential short-range extrapolations for samples with shorter side lengths. However, even at the highest explored density of  $0.1 \text{ \AA}^{-3}$ , our simulations spend very little time at such short distances. At lower densities, pair distances below 2.2 Å are almost completely absent. As another example, consider a collection of four *para*-H<sub>2</sub> molecules where some of the side lengths are very small (around 2.2 Å or shorter) and others are much larger (around 4.5 Å or longer). For such a cluster, the four-body PES produces an interaction energy that is a physically unrealistic linear combination of short-range and long-range interaction energies.<sup>43</sup> However, under these conditions this four-body energy is also typically four to five orders of magnitude smaller than the total two-body and three-body energies of this same cluster, and thus we can easily neglect the inaccuracy.

### C. Sampling strategies

During a simulation, the four-body PES takes longer to evaluate than the three-body PES, which itself takes longer to evaluate than the two-body PES. One reason for this increase in runtime is the combinatoric increase in the number of required terms. When we evaluate a  $k$ -body PES on a system of  $N$  particles, the number of groups of  $k$  particles grows as  $\mathcal{O}(N^k)$ . Another reason the evaluations take longer is that the implementations for the higher-order many-body PESs become more expensive. The two-body PES is implemented using a very fast 1D linear interpolation. The three-body PES is implemented using trilinear interpolation, which requires several times as many calculations as 1D linear interpolation. The four-body PES is implemented using a feed-forward neural network, which is implemented as a repeated sequence of matrix multiplications and activation function calls. The inclusion of the higher-order many-body interaction PESs is expensive enough to the point that simulations under certain conditions become intractable.

We can use approximation sampling strategies to improve the runtime performance of our simulations. Each of the PESs can be used in one of two ways during the simulation; sampling and estimating. During sampling, we use the PESs to calculate the energies for the current and proposed positions for a Monte Carlo step, and use these energies to determine if we accept or reject the proposed position. During estimating, we use the PESs to calculate the total interaction energy of the system, which we use as a sample for the estimator of the total interaction energy. As an approximation, we can choose to omit certain higher-order many-body PESs from the sampling stages of the simulation, but keep them in the estimating stages of the simulation. This approximation assumes that the higher-order many-body interactions have a negligible or perturbative effect on the molecular positions of the *para*-H<sub>2</sub> molecules during sampling. In a study on the effect of three-body interactions in solid helium by Barnes and Hinde,<sup>28</sup> and a study on the effect of three-body interactions in solid *para*-H<sub>2</sub> by this research group,<sup>24</sup> it was shown that this assumption is valid except at very high densities.

With our three PESs, we can define three sampling strategies, each one defined by which of the higher-order many-body PESs are omitted from the sampling phase of the simulation. In the first sampling strategy, labelled by S[2], we use only the two-body PES for the sampling steps. In other words, the potential energy component of the change in energy  $\Delta V$  used to determine if a proposed Monte Carlo step is accepted or rejected is given by

$$\Delta V = V_2(\mathbf{q}_f) - V_2(\mathbf{q}_i), \quad (2)$$

where  $V_2$  is the two-body interaction potential, and  $\mathbf{q}_f$  and  $\mathbf{q}_i$  are the final and initial positions of all molecules in the solid, respectively. In the next sampling strategy,

labelled by S[2, 3], we use only the two-body and three-body PESs for the sampling steps. The potential energy difference during sampling for the S[2, 3] strategy is

$$\Delta V = [V_2(\mathbf{q}_f) + V_3(\mathbf{q}_f)] - [V_2(\mathbf{q}_i) + V_3(\mathbf{q}_i)] . \quad (3)$$

In the last sampling strategy, labelled by S[2, 3, 4], we use the two-body, three-body, and four-body PESs for the sampling steps. The potential energy difference during sampling for the S[2, 3, 4] strategy is

$$\begin{aligned} \Delta V = & [V_2(\mathbf{q}_f) + V_3(\mathbf{q}_f) + V_4(\mathbf{q}_f)] \\ & - [V_2(\mathbf{q}_i) + V_3(\mathbf{q}_i) + V_4(\mathbf{q}_i)] . \end{aligned} \quad (4)$$

The estimation and sampling stages of the simulations are separate from one another. Thus, in each of the S[2], S[2, 3], and S[2, 3, 4] strategies, we can still use all three PESs during the estimation stage. For example, in the S[2] simulations, we only use the two-body PES to calculate the energies for the current and proposed positions during the Monte Carlo steps, but we still use the two-body, three-body, and four-body PESs to calculate the total interaction energies during the estimation stage.

The four-body PES is much more expensive to evaluate compared to the two-body and three-body PESs. For the S[2] and S[2, 3] cases, we are able to reasonably estimate the average four-body potential energy by calling its estimator on only 40 to 50 state snapshots. This is because the variance of the four-body potential energy estimator is relatively small for all densities explored. However, its expensive evaluation time makes the S[2, 3, 4] simulations very slow, and thus we decide to perform them only at the relatively high density of  $0.1 \text{ \AA}^{-3}$ . To perform the S[2, 3, 4] simulations, we take 980 decorrelated position snapshots of the system from a S[2] simulation, and use them as initial positions for 980 separate S[2, 3, 4] simulations. At this density, the S[2] and S[2, 3, 4] simulations have similar acceptance rates for the same Monte Carlo step sizes. To err on the side of caution, each S[2, 3, 4] simulation is run for twice the autocorrelation time of the S[2] simulation before calling the estimators, and only a single estimate is performed before a simulation ends.

We should note that this choice of density was made after having already performed the S[2] and S[2, 3] simulations, with full knowledge that the pressure for the S[2] and S[2, 3] simulation results already exceed the experimental results at this density (see Sec. (IV C)). The emphasis is on choosing a density where we expect the effect of the four-body PES on the solid structure to be very strong, and the change in the radial distribution function (discussed in Sec. (IV D)) to be noticeable.

### III. COMPUTATION

#### A. Path-integral Monte Carlo

Suppose we have a system described by a Hamiltonian  $\hat{H}$  at a finite temperature  $\beta = 1/k_B T$ . The expectation

value of a quantum mechanical operator  $\hat{A}$  in this system can be expressed using the PIMC method as

$$\begin{aligned} \langle \hat{A} \rangle &= \frac{1}{Z} \text{Tr} \left\{ \hat{A} e^{-\beta \hat{H}} \right\} \\ &= \frac{1}{Z} \int d\mathbf{q} d\mathbf{q}' \langle \mathbf{q} | \hat{A} | \mathbf{q}' \rangle \langle \mathbf{q}' | e^{-\beta \hat{H}} | \mathbf{q} \rangle , \end{aligned} \quad (5)$$

where  $Z = \text{Tr} \left\{ \hat{A} e^{-\beta \hat{H}} \right\}$  is the partition function and  $\mathbf{q}$  represents the positions of all particles in the system. We can discretize the integral in imaginary time, writing

$$\langle \mathbf{q}' | e^{-\beta \hat{H}} | \mathbf{q} \rangle = \int \prod_{i=2}^P d\mathbf{q}_i \times \prod_{i=1}^P \langle \mathbf{q}_i | e^{-\tau \hat{H}} | \mathbf{q}_{i+1} \rangle , \quad (6)$$

where  $\tau = \beta/P$  is the imaginary time step, and  $\mathbf{q}_i$  represents the positions of all particles in the system at the imaginary time step with label  $i$ . We also apply the boundary condition  $\mathbf{q}_1 = \mathbf{q}'$  and  $\mathbf{q}_{P+1} = \mathbf{q}$  to Eq. (6). The integral thus forming a ring of coordinates  $\{\mathbf{q}_i\}$ . We use the PIMC method to sample the integral Eq. (5).<sup>59</sup>

Because *para*-H<sub>2</sub> is a boson, our simulation method should in principle account for exchange effects, using a strategy such as the worm algorithm.<sup>60,61</sup> However, previous simulation studies indicate that bosonic exchange between *para*-H<sub>2</sub> molecules is almost completely suppressed in the solid phase.<sup>7,17,62,63</sup> Thus in practice, the *para*-H<sub>2</sub> molecules can be treated as distinguishable particles.

#### B. Trotter error

The PIMC method involves separating the Hamiltonian in Eq. (6) into its potential and kinetic components. Upon doing so, we introduce a systematic Trotter factorization error into our expectation values.<sup>59,64</sup> This systemic error grows with the imaginary time step  $\tau$ . In the limit  $\tau \rightarrow 0$ , or in other words, in the limit of infinitely many time steps, this systemic error vanishes. We account for the Trotter factorization error in the same way that we did in a previous study on the effects of three-body interactions in solid *para*-H<sub>2</sub>.<sup>24</sup>

One method to eliminate the factorization error is the  $\tau$ -extrapolation method. We perform several simulations under the same conditions (the same temperature, density, number of particles, *etc.*), with the only difference between these simulations being the number of time slices  $P$ . Each simulation is run with a different value of  $\tau$ , and produces a different expectation value  $\langle \hat{A} \rangle(\tau)$ . We can fit these expectation values using

$$\langle \hat{A} \rangle(\tau) = \langle \hat{A} \rangle_0 + c_2 \tau^2 + c_4 \tau^4 \quad (7)$$

where  $\langle \hat{A} \rangle_0$  is the expectation value of the observable  $\hat{A}$  in the limit of  $\tau \rightarrow 0$ , and  $c_2$  and  $c_4$  are fit parameters.<sup>64</sup> The  $\tau$ -extrapolation method is ideal when the kinetic and potential energy components are small in magnitude.

Under these conditions, the Trotter factorization error is small, and the extrapolation Eq. (7) is valid even for fairly large values of  $\tau$ . However, as we increase the density of the solid, the kinetic and potential energy components increase in magnitude, and the fit in Eq. (7) becomes less suitable.

Another strategy to mitigate the factorization error is the small- $\tau$  method, where we select a value of  $\tau$  that is small enough such that the Trotter factorization error is tolerably small. This strategy is simpler to implement, but leaves part of the systemic Trotter error in the result.

We use the  $\tau$ -extrapolation method to calculate the energies in a fine grid of densities near the equilibrium density of  $\rho_0 = 0.0261 \text{ \AA}^{-3}$ ,<sup>7,8</sup> where the kinetic and potential energy components are relatively small. For each density, we perform simulations using  $P = \{64, 80, 96, 128, 192\}$  time slices, collect the expectation values for the energies, and use Eq. (7) to find the expectation values in the  $\tau \rightarrow 0$  limit. This method allows us to recover low-variance energies and accurately find the equilibrium density. In the range of densities where we use this  $\tau$ -extrapolation method, the total energies span a range of about  $2 \text{ cm}^{-1}$ , whereas the standard error of the mean of the resulting energies is only on the order of  $0.01 \text{ cm}^{-1}$ .

We use the small- $\tau$  method to calculate the energies of the solid in a sparse grid of densities between  $\rho = 0.024 \text{ \AA}^{-3}$  and  $\rho = 0.1 \text{ \AA}^{-3}$ . We choose  $P = 960$  beads ( $\tau \approx 2.48 \times 10^{-4} \text{ K}^{-1}$ ). In an earlier similar study,<sup>24</sup> it was found that compared to the extrapolated value, this choice of time step leads to a Trotter error in the total energy of about 0.2% at  $\rho = 0.026 \text{ \AA}^{-3}$  and  $\rho = 0.04 \text{ \AA}^{-3}$ , and about 2.5% at  $\rho = 0.1 \text{ \AA}^{-3}$ . Also, at very high densities the simulation results deviate from the experimental data to such an extent that it dwarfs the systemic Trotter error.

### C. Finite system size error

Our simulations of solid *para*-H<sub>2</sub> are done with a finite sized box with periodic boundary conditions applied to each dimension. We must apply the minimum image rules to make sure that we calculate the correct distance between any two molecules. For the two-body PES, we apply the standard minimum image convention. Interactions between any two molecules greater than a cutoff distance of  $L/2$  apart are ignored, where  $L$  is the shortest of the three side lengths of the simulation box. For the three-body PES, we follow the three-body minimum image convention described by Attard.<sup>65</sup> For the four-body PES, we adapt Attard's minimum image convention by ignoring the interaction energy of any four-body geometry where any of the side lengths is greater than  $L/2$ .

Because we perform our simulations within a finite sized simulation box, the potential energy estimators are unable to account for interactions involving molecules outside of this box. As a result, all the potential energy

estimates suffer from a systemic finite system size error. To correct this error we use long-range tail corrections, which are calculations that approximate the interaction energy between a molecule inside of the simulation box and all other molecules outside the simulation box.

The contribution to the two-body interaction energy per molecule beyond a cutoff distance  $L/2$  is given by

$$\epsilon_2^{(t)} = 4\pi \frac{\rho}{2} \int_{L/2}^{\infty} dr r^2 V_2(r) g(r) \quad (8)$$

where  $g(r)$  is the radial pair distribution. The simulation is only able to calculate  $g(r)$  within the cutoff distance. In the pair tail correction, we approximate the radial pair distribution outside the simulation box as being uniform, and set  $g(r) = 1$  in Eq. (8).

We calculate the three-body tail correction using Eq. (2.150) in Ref. [66], which accounts for interactions from all three-body geometries where at least one side length is greater than  $L/2$ . The calculation requires the three-body distribution function, which we approximate using a product of three radial pair distribution functions collected from the simulation.

In an earlier work,<sup>42</sup> we performed S[2] PIMC simulations of solid *para*-H<sub>2</sub> using simulation boxes with both  $N = 180$  particles and  $N = 448$  particles, with the two-body and three-body tail corrections applied to both. The difference between the two total energies, relative to the overall total energy, was less than 0.2% even at the highest densities explored. This was used to verify that  $N = 180$  is a sufficiently large enough number of particles to simulate the solid insofar as energy estimates are concerned.

We do not apply a tail correction for the four-body interaction energy, as we expect it to be negligible. Even at the highest densities considered in this work, where the tail corrections are at their most significant, the two-body and three-body tail corrections for a simulation box of  $N = 180$  particles are less than 1.5% and 0.5% of the total interaction energy, respectively.<sup>42</sup> We know that the magnitude of a tail correction depends on the long-range interaction strength of the corresponding PES. At long distances, the four-body PES decays with  $r^{-12}$ , much more quickly than the two-body PES at  $r^{-6}$  or the three-body PES at  $r^{-9}$ . We can thus expect the four-body tail correction to be even smaller than the three-body tail correction, which itself is already very small.

## IV. RESULTS

### A. Energy components

In Fig. (1), we show how each of the four energy components varies as a function of density in simulations performed using the S[2] strategy. The two-body, three-body, and four-body potential energies all vary exponentially at higher densities, while the kinetic energy increases linearly. Earlier studies on solid *para*-H<sub>2</sub> suggest

that this linear trend for the kinetic energy only holds at lower densities.<sup>17</sup>

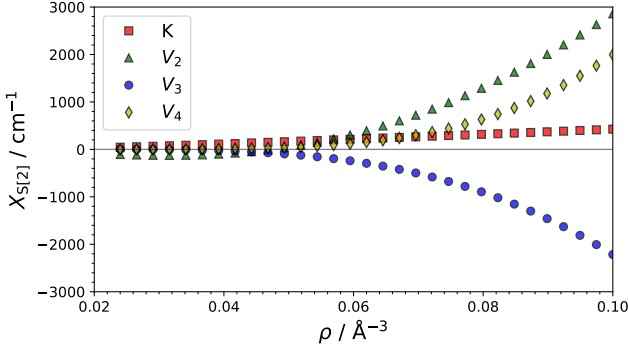


FIG. 1. The energy per particle as a function of the density  $\rho$ , separated into the kinetic (red, squares), two-body potential (green, triangles), three-body potential (blue, circles), and four-body potential (yellow, diamonds) energy components. The simulations are performed using the S[2] sampling strategy. The variable  $X_{S[2]}$  on the vertical axis label is a placeholder for the various energy components. The standard error of the mean of the data is not visible on the scale of the figure.

The inclusion or omission of higher-order many-body interactions during sampling affects the position distribution of the molecules in the solid, which in turn affects estimates of each of the four energy components. To demonstrate this, we perform PIMC simulations of solid *para*-H<sub>2</sub> using both the S[2] and S[2, 3] sampling strategies, for densities between 0.024 Å<sup>-3</sup> and 0.1 Å<sup>-3</sup>. We then take the individual energy components from the S[2, 3] simulations, subtract their counterparts from the S[2] simulations, and plot the differences as a function of density in Fig. (2).

Each of the four energy components experiences a shift when switching from the S[2] strategy to the S[2, 3] strategy. The kinetic and three-body potential energies decrease, while the two-body potential and four-body potential energies increase. For the four-body interaction energy, the trend of the difference increasing reverses at the highest densities explored here. We are unsure of why this is the case. The total energy is almost completely unchanged except near 0.1 Å<sup>-3</sup>, where the difference is just under 0.3% of the total interaction energy. The changes in the individual energy components almost completely cancel each other out.

We can perform a  $\tau$ -extrapolation of the kinetic energy component on its own at  $\rho_0 = 0.0261$  Å<sup>-3</sup>. The predicted average kinetic energy per molecule at the equilibrium density at  $T = 4.2$  K is  $\langle K \rangle = 53.94(1)$  cm<sup>-1</sup> for the S[2] simulations, and  $\langle K \rangle = 52.79(1)$  cm<sup>-1</sup> for the S[2, 3] simulations. Both predictions are greater than the experimental result of 49.3(8) cm<sup>-1</sup> at  $T = 5$  K.<sup>8</sup>

In Table. (I), we show the estimates of the energy components collected from the S[2], S[2, 3], and S[2, 3, 4] simulations performed using  $P = 960$  beads at a density

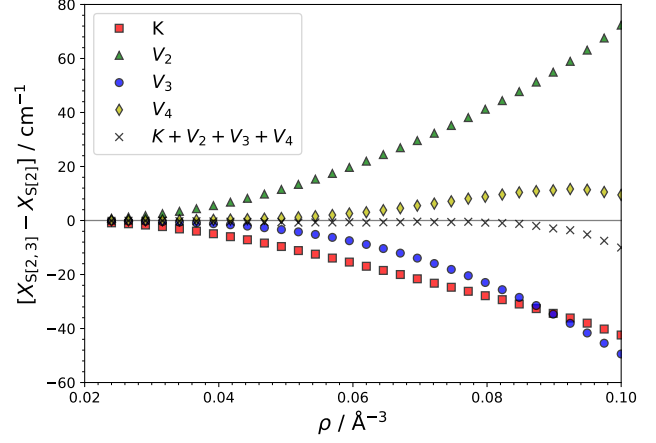


FIG. 2. The difference in the energy per particle as a function of the density  $\rho$ , as collected from the S[2] and S[2, 3] simulations. In addition to the separate kinetic (red, squares), two-body potential (green, triangles), three-body potential (blue, circles), and four-body potential (yellow, diamonds) energy components, we also show the difference between the total energy (black, crosses). The variables  $X_{S[2]}$  and  $X_{S[2,3]}$  on the vertical axis label are placeholders for the energy components collected from S[2] and S[2, 3] simulations, respectively. The standard error of the mean of the data is not visible on the scale of the figure.

TABLE I. In order from top to bottom, estimates of the average kinetic, two-body potential, three-body potential, and four-body potential energy per molecule, followed by the sum of the previous four values. The results are shown from simulations performed under the S[2], S[2, 3], and S[2, 3, 4] sampling strategies, performed at 0.1 Å<sup>-3</sup>. All energies are shown in units of cm<sup>-1</sup>. The two-body and three-body interaction energies have had their respective long-range tail corrections applied.

	S[2]	S[2, 3]	S[2, 3, 4]
$K$	426.969(34)	384.562(41)	361.47(25)
$V_2$	2856.5974(81)	2928.937(13)	3058.842(96)
$V_3$	-2215.1549(35)	-2264.5788(68)	-2324.996(47)
$V_4$	1996.40(11)	2005.88(14)	1999.118(37)
total	3064.81(13)	3054.80(15)	3094.44(27)

of 0.1 Å<sup>-3</sup>. As is the case in the S[2, 3] simulations, the S[2, 3, 4] simulations see a decrease in the kinetic and three-body potential energies, and an increase in the two-body potential energy. However, the shifts are even greater in the S[2, 3, 4] simulations than in the S[2, 3] simulations. The four-body potential energy is very similar in all three sampling cases. The total energy is very similar in all three cases as well, only being about 1% larger in the S[2, 3, 4] case compared to the S[2] case.

## B. Energy-density equation of state

We perform PIMC simulations of solid *para*-H<sub>2</sub> at  $T = 4.2$  K using the S[2] and S[2, 3] sampling strategies. One set of simulations is performed in a fine, regularly spaced grid of densities between  $0.025 \text{ \AA}^{-3}$  and  $0.027 \text{ \AA}^{-3}$ , around the equilibrium density region. For these simulations, we handle the Trotter error using the  $\tau$ -extrapolation method. Another set of simulations is performed in a coarser, regularly spaced grid of densities between  $0.024 \text{ \AA}^{-3}$  and  $0.1 \text{ \AA}^{-3}$ , for which we handle the Trotter error using the small- $\tau$  method.

During the estimation phase, we use the primitive estimator for the kinetic energy, and the standard estimators for the two-body, three-body and four-body interaction potential energies, taking periodic boundary conditions into account. From the estimates, we can create three energy-density curves. One energy-density curve is the sum of only the kinetic and two-body interaction energies, which we label with E[2]. Another is the sum of the kinetic, two-body, and three-body energies, which we label with E[2, 3]. The final is the sum of the kinetic, two-body, three-body, and four-body energies, which we label with E[2, 3, 4].

We can fit the average energy per particle as a function of density for the E[2], E[2, 3], and E[2, 3, 4] cases to a modified Birch equation of state,<sup>67,68</sup>

$$\epsilon = \epsilon_0 - \frac{P_0}{d\rho_0} + \frac{1}{\rho_0} \sum_{n=1}^4 \kappa_n d^{2n/3}, \quad (9)$$

where  $d = \rho/\rho_0$  is the number density normalized by the experimental value of the equilibrium density  $\rho_0 = 0.0261 \text{ \AA}^{-3}$ . This normalization is done to reduce the disparity in the orders of magnitude of the fit parameters. In the supplementary material, we show the fit parameters for the E[2], E[2, 3], and E[2, 3, 4] cases, calculated using both the S[2] and S[2, 3] strategies.

In Fig. (3), we plot the energy-density results collected from simulations performed with the S[2] sampling strategy. These energy-density curves are nearly indistinguishable from those collected from the S[2, 3] simulations. The energy-density curves for the E[2], E[2, 3], and E[2, 3, 4] cases follow the expected trends based on their interaction strengths at short intermolecular separations. For the E[2] curve, the total energy increases as a function of density. The three-body interaction is exponentially attractive at short distances, and when we include it to form the E[2, 3] curve, the total energy decreases. Similarly, the four-body interaction is exponentially repulsive at short distances, and including it to form the E[2, 3, 4] curve causes the total energy to once again increase.

In Fig. (4), we show the energy-density curves from the S[2] simulations around the equilibrium density region. The E[2] and E[2, 3] curves are shifted downwards compared to their counterparts presented in Ref. [24], due to an error in the calculation of the pair tail correction in the earlier work. Even around the equilibrium density,

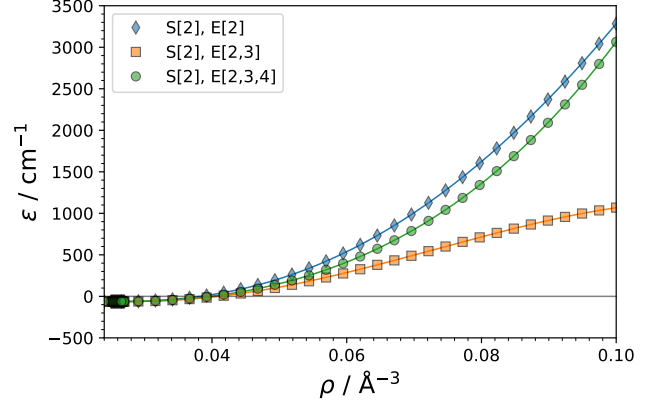


FIG. 3. The energy per molecule  $\epsilon$  as a function of the density  $\rho$  of solid parahydrogen for the E[2] (blue, diamonds), E[2, 3] (orange, squares), and E[2, 3, 4] (green, circles) estimates. All results are shown for simulations performed with the S[2] sampling strategy. The curves are found by fitting the results to Eq. (9). The standard error of the mean of the data is not visible on the scale of the figure.

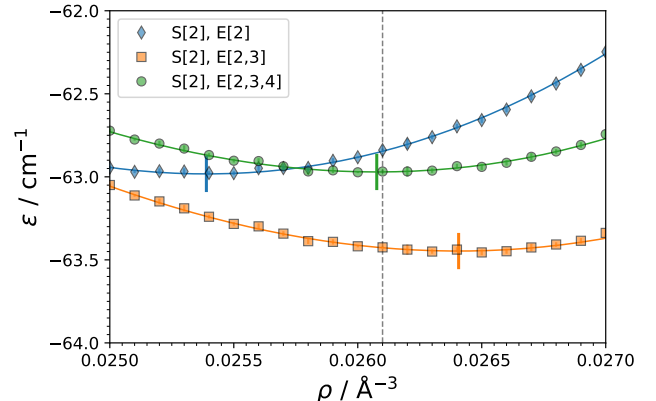


FIG. 4. The energy per molecule  $\epsilon$  as a function of the density  $\rho$  of solid parahydrogen around the equilibrium density for the E[2] (blue, diamonds), E[2, 3] (orange, squares), and E[2, 3, 4] (green, circles) estimates. All results are shown for simulations performed with the S[2] sampling strategy. The short vertical blue, orange, and green lines indicate the equilibrium density predicted by the E[2], E[2, 3], and E[2, 3, 4] estimates, respectively. The vertical dashed line is located at  $\rho_0 = 0.0261 \text{ \AA}^{-3}$ , the experimental result of the equilibrium density.<sup>7,8</sup> The statistical uncertainties are visible within the semitransparent faces of the markers.

where the lattice constant is about  $3.8 \text{ \AA}$ , the three-body and four-body interactions have a small but measurable effect on the total interaction energy. As demonstrated in Fig. (5) for specific geometric configurations, this behaviour would be unreasonable from a classical model of solid *para*-H<sub>2</sub>. At this lattice constant the three-body and four-body interactions are negligibly weak compared to the two-body interaction. However, the large zero-

point quantum displacement of the *para*-H<sub>2</sub> molecules allows their probability distributions to reach distances where these many-body interactions are significant. The predicted equilibrium densities from the S[2] simulations are 0.02539 Å<sup>-3</sup> for the E[2] case, 0.02640 Å<sup>-3</sup> for the E[2, 3] case, and 0.02608 Å<sup>-3</sup> for the E[2, 3, 4] case. The inclusion of the four-body interaction in the total energy estimator improves the prediction of the equilibrium density. The prediction given by the E[2, 3, 4] is closer to the experimental value than either the E[2] or E[2, 3] curves.

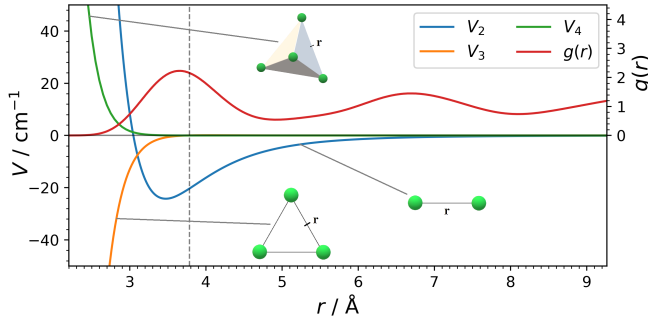


FIG. 5. The radial pair distribution function  $g(r)$  (red) of solid *para*-H<sub>2</sub> at  $\rho_0 = 0.0261 \text{ \AA}^{-3}$ , collected from an S[2] simulation. Also shown are the interaction energies for particular geometries in the *hcp* lattice. We show the two-body potential energy for two *para*-H<sub>2</sub> molecules a distance  $r$  apart (blue), the non-additive three-body potential energy for three *para*-H<sub>2</sub> molecules at the corners of an equilateral triangle of side length  $r$  (orange), and the non-additive four-body potential energy for four *para*-H<sub>2</sub> molecules at the corners of a perfect tetrahedron of side length  $r$  (green). The vertical dashed line shows the position of the lattice constant at this density.

When limited to the energy and density scales relevant near the equilibrium density, the differences in the total energies from the S[2] and S[2, 3] simulations become noticeable, but are still very small. We show the energy-density curves alongside one another in the supplementary material. The predicted equilibrium densities for each of the E[2], E[2, 3], and E[2, 3, 4] estimations are essentially unchanged in the S[2, 3] simulations. Table (II) shows the average energy per molecule at the equilibrium density for each sampling strategy and estimation case. These are in line with estimates from PIMC simulations performed using the Moraldi, Buck, and Silvera-Goldman potentials.<sup>17</sup>

	S[2]	S[2, 3]
E[2]	−62.98(1)	−62.91(2)
E[2, 3]	−63.45(1)	−63.53(2)
E[2, 3, 4]	−62.97(1)	−63.04(2)

TABLE II. The average energy per molecule at the respective equilibrium densities (provided in the text) of each energy-density curve. Values are in units of cm<sup>-1</sup>.

### C. Pressure-density equation of state

We can calculate the pressure as a function of density of solid *para*-H<sub>2</sub> from the energy-density fit Eq. (9) using

$$P = \rho^2 \left. \frac{\partial \epsilon}{\partial \rho} \right|_T = P_0 + \frac{2}{3} \sum_{n=1}^4 n \kappa_n d^{(2n+3)/3}. \quad (10)$$

In Fig. (6), we show the pressure-density curves for simulations performed using the S[2] sampling strategy for the E[2], E[2, 3], and E[2, 3, 4] cases, alongside experimental results.<sup>3,67,69,70</sup> The corresponding pressure-density curves calculated from S[2, 3] simulation results are nearly indistinguishable from those shown in the figure. The E[2] curve overestimates the experimental results even at low densities, which means that the two-body interaction on its own is much too repulsive. From the E[2, 3] curve, we can see that including the attractive three-body interaction decreases the pressure. However, the three-body interaction overcorrects the repulsion from the two-body interaction, to the extent that at the highest densities we see unphysical results where the pressure decreases with density. From the E[2, 3, 4] curve, we see that including the four-body interactions in the estimate for the total energy once again increases the pressure, and drastically improves the agreement between simulation and experimental results up to around 0.065 Å<sup>-3</sup>. As we move to higher densities, the four-body interaction once again overestimates the pressure compared to the experimental data.

The effect seen here, in which the inclusion of three-body interactions causes an underestimation of the pressure with respect to the experimental data, has also been seen in quantum Monte Carlo simulations of solid helium. Barnes and Hinde found that the combination of the two-body Aziz potential<sup>71</sup> and the three-body Cencek potential<sup>72</sup> causes an underestimation of the pressure at high densities.<sup>28</sup> Chang and Boninsegni, performed PIMC simulations of solid helium using two separate pairs of two-body and three-body interaction potentials,<sup>73–76</sup> and found in both cases that the simulation results underestimated the pressure.<sup>77</sup>

### D. Radial pair distribution function

The inclusion of higher-order many-body interactions during sampling affects the structure of the solid. To see this change, we can look at the radial pair distribution function  $g(r)$ , whose (un-normalized) estimator in the simulation is given by

$$\hat{g}(r) = \left\langle \sum_{n < m}^N \sum_i^P \delta(r - |\mathbf{r}_{i,n} - \mathbf{r}_{i,m}|) \right\rangle, \quad (11)$$

where  $\mathbf{r}_{i,n}$  is the position of the bead at the timeslice with index  $i$  and the particle with index  $n$ . We can also look at

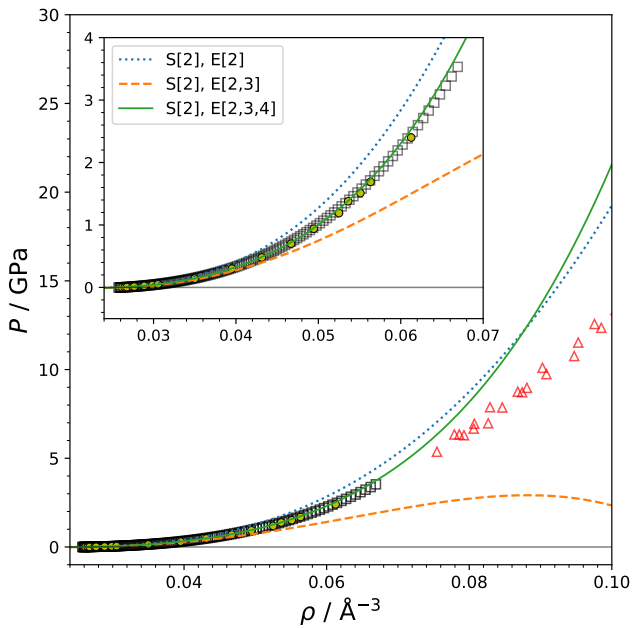


FIG. 6. The pressure  $P$  as a function of the density  $\rho$  of solid parahydrogen for the E[2] (blue, dotted line), E[2,3] (orange, dashed line), and E[2,3,4] (green, solid line) estimates. The curves are calculated using Eq. (10). Also shown are experimentally derived results from Ref. [69] (solid yellow, circles), Refs. [3,67] (black, squares), and Ref. [70] (red, triangles).

the centroid radial pair distribution function  $g_c(r)$ , whose (un-normalized) estimator is given by

$$\hat{g}_c(r) = \left\langle \sum_{n < m}^N \delta(r - |\mathbf{c}_n - \mathbf{c}_m|) \right\rangle, \quad (12)$$

where  $\mathbf{c}_n$  is the centroid of the particle with index  $n$ , given by

$$\mathbf{c}_n = \frac{1}{P} \sum_{i=1}^P \mathbf{r}_{i,n}. \quad (13)$$

In Fig. (7), we show the normalized radial pair distribution function  $g(r)$  of the S[2], S[2,3], and S[2,3,4] simulations at  $0.1 \text{ \AA}^{-3}$ . In Fig. (8), we show the normalized centroid radial pair distribution function  $g_c(r)$  under the same conditions. All three sampling strategies produce similar distributions.

In an earlier study,<sup>24</sup> we found that the distribution of the distances from each bead to the centroid of their corresponding molecule,

$$\hat{c}(r) = \left\langle \sum_{n=1}^N \sum_{i=1}^P \delta(r - |\mathbf{r}_{i,n} - \mathbf{c}_n|) \right\rangle, \quad (14)$$

is essentially unchanged between the S[2] and S[2,3] simulations. Our current simulations reproduce the same curves as found in Fig. (10) of Ref. [24]. Our estimate

of Eq. (14) for the S[2,3,4] simulations at  $0.1 \text{ \AA}^{-3}$  is the same as that from the S[2] and S[2,3] simulations. This indicates that the many-body interactions do not change the overall quantum mechanical “spreading” of each individual molecule.

The  $g(r)$  curve from the S[2,3] simulation is slightly flatter and wider than the  $g(r)$  curve from the S[2] simulation around the first shell. From the second shell onwards, the S[2] and S[2,3] results are nearly indistinguishable. The  $g_c(r)$  curve for the S[2,3] simulation is also slightly wider than that of the S[2] simulation around the first shell. This indicates that the three-body potential softens the total interaction in such a way that the centroid of each molecule has a greater translational displacement about its nominal lattice site, but the quantum mechanical “spreading” of each molecule does not increase.

Given that the widening of the  $g(r)$  distribution when moving from the S[2] case to the S[2,3] case is likely caused by the attractive interaction energy of the three-body PES, it is surprising to see that the  $g(r)$  distribution widens even further in the S[2,3,4] case, when the strongly repulsive four-body PES is included. This softening of the  $g(r)$  distribution is also pronounced beyond the first shell. Looking at the  $g_c(r)$  curves in the inset of Fig. (8), the cause becomes apparent.

The four-body PES used in this work is a function of all six relative pair distances between the four molecules. Although the relationship between the six side lengths and the interaction energy is fairly complicated, as a general rule, we can decrease the four-body interaction energy by increasing the average side length.<sup>43</sup> Consider a cluster of four *para*-H<sub>2</sub> molecules, one at each corner of a perfect tetrahedron. We can lower the total interaction energy of this cluster by moving two of the molecules slightly closer together, and the other two molecules slightly farther apart, in a way that causes the average side length of the cluster to increase. This trend also applies to geometries found in the *hcp* lattice other than the perfect tetrahedron. In other words, we decrease the four-body interaction energy by having certain pairs of molecules move slightly closer together, and other pairs of molecules move slightly farther apart, which causes the translational symmetry breaking in the *hcp* lattice. This is why including the four-body PES during sampling causes the peaks in the  $g(r)$  curve to widen, and the peaks in the  $g_c(r)$  curve to slightly split.

The translational symmetry breaking in the *hcp* lattice introduced by the S[2,3,4] simulations is very likely to be a simulation artifact. We should remind the readers that these simulations are done at  $0.1 \text{ \AA}^{-3}$ , whereas Fig. (6) shows that the simulations predict pressures that exceed the experimental results beyond around  $0.065 \text{ \AA}^{-3}$ . At such high densities, many-body interactions beyond the four-body interaction become significant. It is possible that this symmetry breaking would vanish if five-body and even higher-order many-body interactions were included in these simulations at this density.

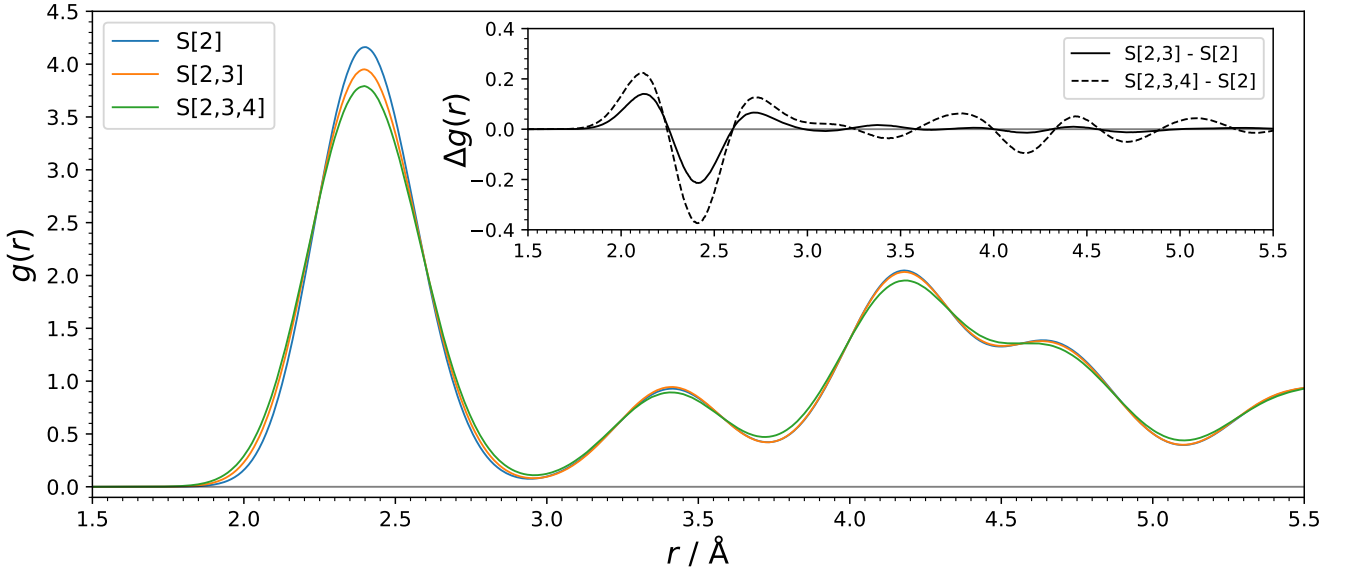


FIG. 7. The radial pair distribution function  $g(r)$  of solid parahydrogen at a density of  $\rho = 0.1 \text{ \AA}^{-3}$ , collected from simulations performed using the S[2] (blue), S[2,3] (orange), and S[2,3,4] (green) sampling strategies. The estimates are done using Eq. (11). In the inset, we show the differences between the  $g(r)$  curves from the S[2,3] and S[2] simulations (black, solid), and from the S[2,3,4] and S[2] simulations (black dashed).

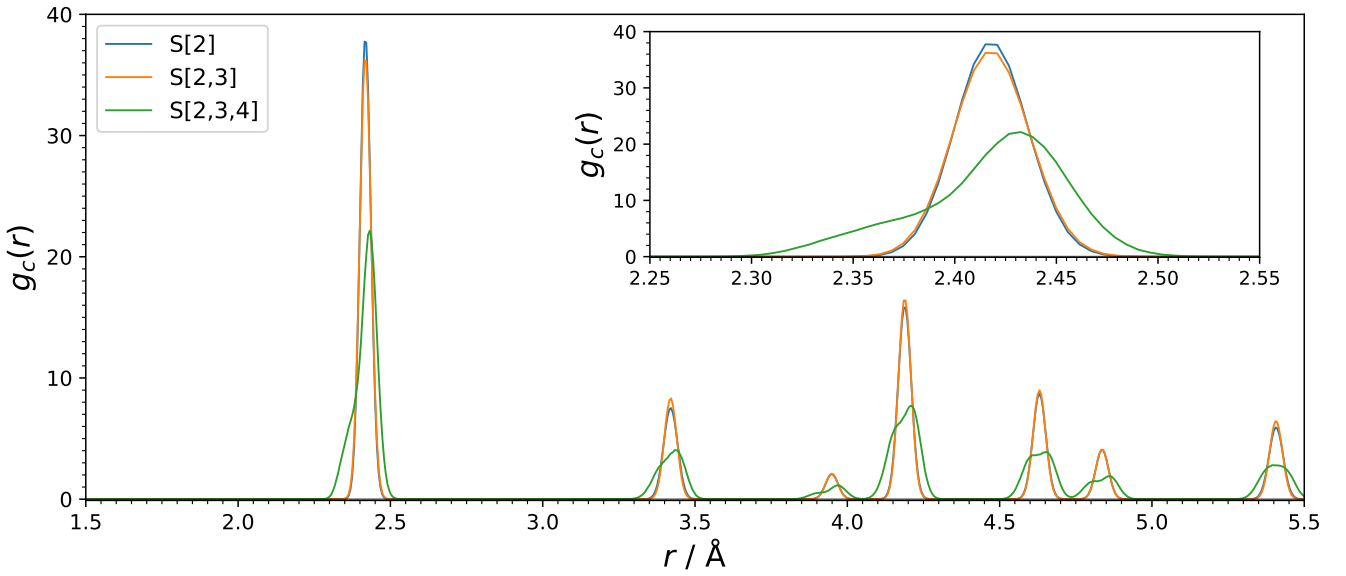


FIG. 8. The centroid radial pair distribution function  $g_c(r)$  of solid parahydrogen at a density of  $\rho = 0.1 \text{ \AA}^{-3}$ , collected from simulations performed using the S[2] (blue), S[2,3] (orange), and S[2,3,4] (green) sampling strategies. The estimates are done using Eq. (12). In the inset, we zoom into the curve around the first shell.

Like the S[2,3,4] simulations, the predicted pressure-density relationship by the S[2,3] simulations deviate greatly from the experimental data at  $0.1 \text{ \AA}^{-3}$ . However, the S[2,3] simulations do not introduce a symmetry breaking effect, despite also lacking higher-order many-body interactions. A possible reason for this discrepancy might be the fact that the four-body PES is a function

of six pair distances, whereas the three-body PES is a function of only three pair distances. Because the four-body PES has more degrees of freedom, the molecules in the solid are able to deviate from their ideal *hcp* lattice positions in a way that causes symmetry breaking and decreases the total four-body interaction energy. In contrast, the three-body PES may not have enough de-

grees of freedom for this to occur, causing the molecules to remain around their ideal *hcp* lattice positions.

## V. CONCLUSION

In this work, we performed PIMC simulations of solid parahydrogen using *ab initio* two-body, three-body, and four-body PESs. We found that simulations that use the *ab initio* two-body, three-body, and four-body interaction energy estimators reproduce the experimental pressure-density results very well below densities of about  $0.065 \text{ \AA}^{-3}$ . In particular, the agreement between the simulation and experimental results jumps drastically going from the E[2, 3] to the E[2, 3, 4] case. The three-body and four-body PESs affect the energy-density relationship of solid parahydrogen even at densities as low as  $0.024 \text{ \AA}^{-3}$ . The E[2, 3, 4] case gives a prediction of the equilibrium density that is much closer to the experimental result than either the E[2] and E[2, 3] cases.

We investigated the use of strategies that include or omit the many-body interactions during sampling as a way to improve the simulation performance. When we switch from the S[2] to the S[2, 3] strategy, each of the energy components experiences a shift, but these changes cancel each other out in such a way that the total interaction energy is nearly unchanged. Compared to the S[2] simulation, the S[2, 3] simulation gives an estimate of the average kinetic energy per molecule at equilibrium density that is slightly closer to experiment. Including the three-body PES during sampling causes very slight changes in the structure of the solid. At the relatively high density of  $0.1 \text{ \AA}^{-3}$ , further including the four-body PES introduces translational symmetry breaking in the *hcp* lattice. This symmetry breaking is likely a simulation artifact, and might be best described as a cautionary tale against using many-body interactions at densities where even higher-order many-body interactions are significant.

The most likely means of improving the simulation results at higher densities would be to include five-body and higher-order many-body interaction energies. Tian *et al.* performed a computational study on effects of many-body interactions on the EOS of solid  ${}^4\text{He}$ , up to the six-body interaction.<sup>27</sup> They found that, at high densities, the even-parity (two-body, four-body, six-body) interactions are overall repulsive, while the odd-parity (three-body and five-body) interactions are overall attractive. Each successive many-body interaction has a weaker overall contribution to the total interaction energy. Their model for the pressure-density EOS of solid helium showed greater agreement with the experimental results with each successive higher-order many-body interaction. It is reasonable to assume that similar improvements can be seen in solid parahydrogen.

However, there are a number of challenges with including *ab initio* higher-order many-body interactions in a non-additive fashion as has been done in this work. The electronic structure calculations needed to create the

training data become much more expensive as more hydrogen molecules are included. More drastic approximations may be required to create the *ab initio* five-body and higher-order many-body PESs. For example, one might ignore the Counterpoise correction, use a lower-quality calculation method, use a smaller basis set, or focus only on certain geometries that contribute the most to the solid. In addition, the evaluation of the total interaction energy during the estimation step becomes much more expensive. It is likely that an entirely different approach to including the many-body interaction energies will need to be explored.

The lack of further higher-order many-body interactions cannot explain all the shortcomings of the simulation results. For example, the higher-order many-body interactions are extremely weak at low densities, and thus we cannot use their absence to explain the deviation between the predicted and experimental kinetic energy per molecule at the equilibrium density. Another way to improve the results would be to switch from using isotropic PESs, to PESs that include more degrees of freedom.

## SUPPLEMENTARY MATERIAL

Refer to the supplementary material for descriptions of the fit parameters for the modified Birch equation of state, the energy-density curves near equilibrium for the S[2] and S[2, 3] simulations, and the energy-density data used to create the equations of state in this paper.

## DATA AVAILABILITY

The data that supports the findings of this study are available within the article and its supplementary material.

## ACKNOWLEDGEMENTS

The authors acknowledge the Natural Sciences and Engineering Research Council (NSERC) of Canada (RGPIN-2016-04403), the Ontario Ministry of Research and Innovation (MRI), the Canada Research Chair program (950-231024), and the Canada Foundation for Innovation (CFI) (project No. 35232). A. I. acknowledges the support of the NSERC of Canada (CGSD3-558762-2021).

## REFERENCES

- <sup>1</sup>H. P. Gush, W. F. J. Hare, E. J. Allin, and H. L. Welsh, “The infrared fundamental band of liquid and solid hydrogen,” *Can. J. Phys.*, vol. 38, p. 176, 1960.
- <sup>2</sup>L. H. Nosanow, “Theory of quantum crystals,” *Phys. Rev.*, vol. 146, p. 120, 1966.

- <sup>3</sup>I. F. Silvera, "The solid molecular hydrogens in the condensed phase: Fundamentals and static properties," *Rev. Mod. Phys.*, vol. 52, p. 393, 1980.
- <sup>4</sup>A. Bhandari, A. P. Rollings, L. Ratto, and J. D. Weinstein, "High-purity solid parahydrogen," *Rev. Sci. Instr.*, vol. 92, p. 073202, 2021.
- <sup>5</sup>C. S. Barrett, L. Meyer, and J. Wasserman, "Crystal structure of solid hydrogen and deuterium, and of neon-hydrogen and neon-deuterium mixtures," *J. Chem. Phys.*, vol. 45, p. 834, 1966.
- <sup>6</sup>O. Schnepp, "One-phonon excited states of solid H<sub>2</sub> and D<sub>2</sub> in the ordered phase," *Phys. Rev. A*, vol. 2, no. 6, p. 2574, 1970.
- <sup>7</sup>M. Dusseault and M. Boninsegni, "Atomic displacements in quantum crystals," *Phys. Rev. B*, vol. 95, p. 104518, 2017.
- <sup>8</sup>T. R. Prisk, R. T. Azuah, D. L. Abernathy, G. E. Granroth, T. E. Sherline, P. E. Sokol, J. Hu, and M. Boninsegni, "Zero-point motion of liquid and solid hydrogen," *Phys. Rev. B*, vol. 107, p. 094511, 2023.
- <sup>9</sup>F. Fernández-Alonso, C. Cabrillo, R. Fernández-Perea, F. J. Bermejo, M. A. González, C. Mondelli, and E. Farhi, "Solid *para*-hydrogen as the paradigmatic quantum crystal: Three observables probed by ultrahigh-resolution neutron spectroscopy," *Phys. Rev. B*, vol. 86, p. 144524, 2012.
- <sup>10</sup>U. Buck, F. Huisken, A. Kohlhase, D. Otten, and J. Schaefer, "State resolved rotational excitation in D<sub>2</sub> + H<sub>2</sub> collisions," *J. Chem. Phys.*, vol. 78, p. 4439, 1978.
- <sup>11</sup>I. F. Silvera and V. V. Goldman, "The isotropic intermolecular potential for H<sub>2</sub> and D<sub>2</sub> in the solid and gas phases," *J. Chem. Phys.*, vol. 69, p. 4209, 1978.
- <sup>12</sup>M. J. Norman, R. O. Watts, and U. Buck, "A spherical potential for hydrogen from solid state and scattering data," *J. Chem. Phys.*, vol. 81, p. 3500, 1984.
- <sup>13</sup>P. Diep and J. K. Johnson, "An accurate H<sub>2</sub>–H<sub>2</sub> interaction potential from first principles," *J. Chem. Phys.*, vol. 112, no. 10, p. 4465, 2000.
- <sup>14</sup>R. J. Hinde, "A six-dimensional H<sub>2</sub>–H<sub>2</sub> potential energy surface for bound state spectroscopy," *J. Chem. Phys.*, vol. 128, p. 154308, 2008.
- <sup>15</sup>K. Patkowski, W. Cencek, P. Jankowski, K. Szalewicz, J. B. Mehl, G. Garberoglio, and A. H. Harvey, "Potential energy surface for interactions between two hydrogen molecules," *J. Chem. Phys.*, vol. 129, p. 094304, 2008.
- <sup>16</sup>N. Faruk, M. Schmidt, H. Li, R. J. Le Roy, and P.-N. Roy, "First-principles prediction of the Raman shifts in parahydrogen clusters," *J. Chem. Phys.*, vol. 141, p. 014310, 2014.
- <sup>17</sup>T. Omiyinka and M. Boninsegni, "Pair potentials and equation of state of solid *para*-hydrogen to megabar pressure," *Phys. Rev. B*, vol. 88, p. 024112, 2013.
- <sup>18</sup>F. Operetto and F. Pederiva, "Diffusion Monte Carlo study of the equation of state of solid para-H<sub>2</sub>," *Phys. Rev. B*, vol. 73, p. 184124, 2006.
- <sup>19</sup>M. J. Elrod and R. J. Saykally, "Many-body effects in intermolecular forces," *Chem. Rev.*, vol. 94, p. 1975, 1994.
- <sup>20</sup>A. O. de-la Roza, L. M. LeBlanc, and E. R. Johnson, "What is "many-body" dispersion and should I worry about it?," *Phys. Chem. Chem. Phys.*, vol. 22, pp. 8266–8276, 2020.
- <sup>21</sup>P. Wind and I. Røeggen, "Ab initio calculation of three-body interaction in the (H<sub>2</sub>)<sub>3</sub> trimer," *Chem. Phys.*, vol. 211, pp. 179–189, 1996.
- <sup>22</sup>R. J. Hinde, "Three-body interactions in solid parahydrogen," *Chem. Phys. Lett.*, vol. 460, pp. 141–145, 2008.
- <sup>23</sup>S. Manzhos, K. Nakai, and K. Yamashita, "Three-body interactions in clusters CO–(pH<sub>2</sub>)<sub>n</sub>," *Chem. Phys. Lett.*, vol. 493, pp. 229–233, 2010.
- <sup>24</sup>A. Ibrahim and P.-N. Roy, "Equation of state of solid parahydrogen using *ab initio* two-body and three-body interaction potentials," *J. Chem. Phys.*, vol. 157, p. 174503, 2022.
- <sup>25</sup>W. Cencek, G. Garberoglio, A. H. Harvey, M. O. McLinden, and K. Szalewicz, "Three-body nonadditive potential for argon with estimated uncertainties and third virial coefficient," *J. Phys. Chem. A*, vol. 117, pp. 7542–7552, 2013.
- <sup>26</sup>K. Rościszewski, B. Paulus, P. Fulde, and H. Stoll, "Ab *initio* coupled-cluster calculations for the fcc and hcp structures of rare-gas solids," *Phys. Rev. B*, vol. 62, no. 9, p. 5482, 2000.
- <sup>27</sup>C.-L. Tian, F.-S. Liu, F.-Q. Jing, and L.-C. Cai, "Five- and six-body effects on equation of state of solid <sup>4</sup>He," *J. Phys. Condens. Matter*, vol. 18, pp. 8103–8112, 2006.
- <sup>28</sup>A. L. Barnes and R. J. Hinde, "Effect of three-body interactions on the zero-temperature equation of state of HCP solid <sup>4</sup>He," *J. Chem. Phys.*, vol. 146, p. 094510, 2017.
- <sup>29</sup>G. Garberoglio, A. H. Harvey, J. Lang, M. Przybytek, M. Lesiuk, and B. Jeziorski, "Path-integral calculation of the third dielectric virial coefficient of helium based on *ab initio* three-body polarizability and dipole surfaces," *J. Chem. Phys.*, vol. 161, p. 144111, 2024.
- <sup>30</sup>D. Binosi, G. Garberoglio, and A. H. Harvey, "Third density and acoustic virial coefficients of helium isotopologues from *ab initio* calculations," *J. Chem. Phys.*, vol. 160, p. 244305, 2024.
- <sup>31</sup>P. Marienhagen and K. Meier, "Calculation of thermodynamic properties of helium using path integral Monte Carlo simulations in the *NpT* ensemble and *ab initio* potentials," *J. Chem. Phys.*, vol. 161, p. 224110, 2024.
- <sup>32</sup>P. Schwerdtfeger and A. Hermann, "Equation of state for solid neon from quantum theory," *Phys. Rev. B*, vol. 80, p. 064106, 2009.
- <sup>33</sup>G. Garberoglio, "On the contribution of non-additive three-body interactions to the third virial coefficient of *para*-hydrogen," *Chem. Phys. Lett.*, vol. 557, p. 26, 2013.
- <sup>34</sup>T. W. Maltby, M. Hammer, and Ø. Wilhelmsen, "Equation of state for solid argon valid for temperatures up to 300 K and pressures up to 16 GPa," *J. Phys. Chem. Ref. Data*, vol. 53, p. 043102, 2024.
- <sup>35</sup>C.-L. Tian, N. Wu, F. Liu, S. K. Saxena, and X. Zheng, "Four-body interaction energy for compressed solid krypton from quantum theory," *J. Chem. Phys.*, vol. 137, p. 044108, 2012.
- <sup>36</sup>R. J. Wheatley, G. Garberoglio, and A. H. Harvey, "Four-body nonadditive potential energy surface and the fourth virial coefficient of helium," *J. Chem. Eng. Data.*, vol. 68, pp. 3257–3264, 2023.
- <sup>37</sup>T. Morresi and G. Garberoglio, "Revisiting the properties of superfluid and normal liquid <sup>4</sup>He using *ab initio* potentials," *J. Low Temp. Phys.*, 2025.
- <sup>38</sup>A. Paszke, S. Gross, F. Massa, A. Lerer, J. Bradbury, G. Chanan, T. Killeen, Z. Lin, N. Gimelshein, L. Antiga, A. Desmaison, A. Kopf, E. Yang, Z. DeVito, M. Raison, A. Tejani, S. Chilamkurthy, B. Steiner, L. Fang, J. Bai, and S. Chintala, "PyTorch: an imperative style, high-performance deep learning library," in *Advances in Neural Information Processing Systems 32*, pp. 8024–8035, Curran Associates, Inc., 2019.
- <sup>39</sup>M. Abadi, A. Agarwal, P. Barham, E. Brevdo, Z. Chen, C. Citro, G. S. Corrado, A. Davis, J. Dean, M. Devin, S. Ghemawat, I. Goodfellow, A. Harp, G. Irving, M. Isard, Y. Jia, R. Jozefowicz, L. Kaiser, M. Kudlur, J. Levenberg, D. Mané, R. Monga, S. Moore, D. Murray, C. Olah, M. Schuster, J. Shlens, B. Steiner, I. Sutskever, K. Talwar, P. Tucker, V. Vanhoucke, V. Vasudevan, F. Viégas, O. Vinyals, P. Warden, M. Wattenberg, M. Wicke, Y. Yu, and X. Zheng, "TensorFlow: Large-scale machine learning on heterogeneous systems," 2015. Software available from tensorflow.org.
- <sup>40</sup>R. S. Graham and R. J. Wheatley, "Machine learning for non-additive intermolecular potentials: Quantum chemistry to first-principles predictions," *Chem. Commun.*, vol. 58, p. 6898, 2022.
- <sup>41</sup>J. Broad, S. Preston, R. J. Wheatley, and R. S. Graham, "Gaussian process models of potential energy surfaces with boundary optimization," *J. Chem. Phys.*, vol. 155, p. 144106, 2021.
- <sup>42</sup>A. Ibrahim and P.-N. Roy, "Three-body potential energy surface for *para*-hydrogen," *J. Chem. Phys.*, vol. 156, p. 044301, 2022.
- <sup>43</sup>A. Ibrahim and P.-N. Roy, "A neural network-based four-body potential energy surface for parahydrogen," *J. Chem. Phys.*, vol. 160, p. 244308, 2024.

- <sup>44</sup>E. Gregoryanz, C. Ji, P. Dalladay-Simpson, B. Li, R. T. Howie, and H.-K. Mao, “Everything you always wanted to know about metallic hydrogen but were afraid to ask,” *Matter Radiat. Extremes*, vol. 5, p. 038101, 2020.
- <sup>45</sup>D. Marx and M. H. Müser, “Path integral simulations of rotors: Theory and applications,” *J. Phys. Condens. Matter*, vol. 11, p. R117, 1999.
- <sup>46</sup>I. Goncharenko and P. Loubeyre, “Neutron and X-ray diffraction study of the broken symmetry phase transition in solid deuterium,” *Nature*, vol. 435, pp. 1206–1209, 2005.
- <sup>47</sup>D. M. Ceperley and B. J. Alder, “Ground state of solid hydrogen at high pressures,” *Phys. Rev. B*, vol. 36, pp. 2092–2106, 1987.
- <sup>48</sup>M. Schmidt, J. M. Fernández, N. Faruk, M. Nooijen, R. J. Le Roy, J. H. Morilla, G. Tejeda, S. Montero, and P.-N. Roy, “Raman vibrational shifts of small clusters of hydrogen isotopologues,” *J. Phys. Chem. A*, vol. 119, p. 12551, 2015.
- <sup>49</sup>H. Li, P.-N. Roy, and R. J. Le Roy, “An “adiabatic-hindered-rotor” treatment allows *para*-H<sub>2</sub> to be treated as if it were spherical,” *J. Chem. Phys.*, vol. 133, p. 104305, 2010.
- <sup>50</sup>H. Li, P.-N. Roy, and R. J. Le Roy, “Analytic Morse/long-range potential energy surfaces and predicted infrared spectra for CO<sub>2</sub>–H<sub>2</sub>,” *J. Chem. Phys.*, vol. 132, no. 21, p. 214309, 2010.
- <sup>51</sup>L. Wang, D. Xie, R. J. Le Roy, and P.-N. Roy, “A new four-dimensional *ab initio* potential energy surface for N<sub>2</sub>O–He and vibrational band origin shifts for the N<sub>2</sub>O–He<sub>N</sub> clusters with  $N = 1 - 40$ ,” *J. Chem. Phys.*, vol. 137, p. 104311, 2012.
- <sup>52</sup>L. Wang, D. Xie, R. J. Le Roy, and P.-N. Roy, “A new six-dimensional potential energy surface for H<sub>2</sub>–N<sub>2</sub>O and its adiabatic-hindered-rotor treatment,” *J. Chem. Phys.*, vol. 139, p. 034312, 2013.
- <sup>53</sup>H. Li, X.-L. Zhang, R. J. Le Roy, and P.-N. Roy, “Analytic Morse/long-range potential energy surfaces and predicted infrared spectra for CO–H<sub>2</sub> dimer and frequency shifts of CO in (*para*-H<sub>2</sub>)<sub>N</sub>  $N = 1 - 20$  clusters,” *J. Chem. Phys.*, vol. 139, p. 164315, 2013.
- <sup>54</sup>A. Marr, T. Halverson, A. Tripp, and P.-N. Roy, “Vibrational Raman shifts of spin isomer combinations of hydrogen dimers and isotopologues,” *J. Phys. Chem. A*, vol. 124, no. 34, pp. 6877–6888, 2020.
- <sup>55</sup>M. Schmidt and P.-N. Roy, “On the accuracy and efficiency of different methods to calculate raman vibrational shifts of parahydrogen clusters,” *J. Chem. Phys.*, vol. 156, p. 084102, 2022.
- <sup>56</sup>MRCC, a quantum chemical program suite written by M. Kállay and P. R. Nagy and D. Mester and L. Gyevi-Nagy and J. Csóka and P. B. Szabó and Z. Rolik and G. Samu and J. Csontos and B. Hégly and Á. Ganyecz and I. Ladjánszki and L. Szegedy and B. Ladóczki and K. Petrov and M. Farkas and P. D. Mezei and R. A. Horbáth. See [www.mrcc.hu](http://www.mrcc.hu).
- <sup>57</sup>M. Kállay, P. R. Nagy, D. Mester, Z. Rolik, G. Samu, J. Csontos, J. Csóka, P. B. Szabó, L. Gyevi-Nagy, B. Hégly, I. Ladjánszki, L. Szegedy, B. Ladóczki, K. Petrov, M. Farkas, P. D. Mezei, and Á. Ganyecz, “The MRCC program system: Accurate quantum chemistry from water to proteins,” *J. Chem. Phys.*, vol. 152, p. 074107, 2020.
- <sup>58</sup>O. T. Unke, S. Chmiela, H. E. Sauceda, M. Gastegger, I. Poltavsky, K. T. Schütt, A. Tkatchenko, and K.-R. Müller, “Machine learning force fields,” *Chem. Rev.*, vol. 121, pp. 10142–10186, 2021.
- <sup>59</sup>D. M. Ceperley, “Path integrals in the theory of condensed helium,” *Rev. Mod. Phys.*, vol. 67, p. 279, 1995.
- <sup>60</sup>M. Boninsegni, N. V. Prokof'ev, and B. V. Svistunov, “Worm algorithms for continuous-space path integral Monte Carlo simulations,” *Phys. Rev. Lett.*, vol. 96, p. 070601, 2006.
- <sup>61</sup>M. Boninsegni, N. V. Prokof'ev, and B. V. Svistunov, “Worm algorithm and diagrammatic Monte Carlo: A new approach to continuous-space path integral Monte Carlo simulations,” *Phys. Rev. E*, vol. 74, p. 036701, 2006.
- <sup>62</sup>M. Boninsegni, “Search for superfluidity in supercooled liquid parahydrogen,” *Phys. Rev. B*, vol. 97, p. 054517, 2018.
- <sup>63</sup>A. Ibrahim, L. Wang, T. Halverson, R. J. Le Roy, and P.-N. Roy, “Equation of state and first principles prediction of the vibrational matrix shift of solid parahydrogen,” *J. Chem. Phys.*, vol. 151, p. 244501, 2019.
- <sup>64</sup>Y. Yan and D. Blume, “Path integral Monte Carlo ground state approach: Formalism, implementation, and applications,” *J. Phys. B*, vol. 50, p. 223001, 2017.
- <sup>65</sup>P. Attard, “Pair-hypernetted-chain closure for three-body potentials: Results for argon with the Axilrod-Teller triple-dipole potential,” *Phys. Rev. A*, vol. 45, no. 6, pp. 3659–3669, 1991.
- <sup>66</sup>M. P. Allen and D. J. Tildesley, *Computer simulation of liquids*. Oxford University Press, 2 ed., 2017.
- <sup>67</sup>A. Driessens, J. A. de Waal, and I. F. Silvera, “Experimental determination of the equation of state of solid hydrogen and deuterium at high pressures,” *J. Low Temp. Phys.*, vol. 34, p. 255, 1979.
- <sup>68</sup>R. E. Cohen, O. Gölseren, and R. J. Hemley, “Accuracy of equation-of-state formulations,” *Am. Mineral.*, vol. 85, pp. 338–344, 2000.
- <sup>69</sup>S. N. Ishmaev, I. P. Sadikov, A. A. Chernyshov, B. A. Vindryaevskii, V. A. Sukhoparov, A. S. Telepnev, and G. V. Kobelev, “Neutron structural investigations of solid parahydrogen at pressures up to 24 kbar,” *Zh. Eksp. Teor. Fiz.*, vol. 84, pp. 394–403, 1983.
- <sup>70</sup>H. Mao and R. J. Hemley, “Ultrahigh-pressure transitions in solid hydrogen,” *Rev. Mod. Phys.*, vol. 66, pp. 671–692, 1994.
- <sup>71</sup>R. A. Aziz, F. R. W. McCourt, and C. C. K. Wong, “A new determination of the ground state interatomic potential for He<sub>2</sub>,” *Mol. Phys.*, vol. 61, pp. 1487–1511, 1987.
- <sup>72</sup>W. Cencek, K. Patkowski, and K. Szalewicz, “Full-configuration interaction calculation of three-body nonadditive contribution to helium interaction potential,” *J. Chem. Phys.*, vol. 131, p. 064105, 2009.
- <sup>73</sup>R. A. Aziz, V. P. S. Nain, J. S. Carley, W. L. Taylor, and G. T. McConville, “An accurate intermolecular potential for helium,” *J. Chem. Phys.*, vol. 70, pp. 4330–4342, 1979.
- <sup>74</sup>L. W. Bruch and I. J. McGee, “Calculations and estimates of the ground state energy of helium trimers,” *J. Chem. Phys.*, vol. 59, pp. 409–413, 1973.
- <sup>75</sup>A. R. Janzen and R. A. Aziz, “An accurate potential energy curve for helium based on *ab initio* calculations,” *J. Chem. Phys.*, vol. 107, pp. 914–919, 1997.
- <sup>76</sup>M. J. Cohen and J. N. Murrell, “An analytic function for the three-body potential of He<sub>3</sub>,” *Chem. Phys. Lett.*, vol. 260, pp. 371–376, 1996.
- <sup>77</sup>S.-Y. Chang and M. Boninsegni, “*Ab initio* potentials and the equation of state of condensed helium at high pressure,” *J. Chem. Phys.*, vol. 115, pp. 2629–2633, 2001.

# Supplementary Information for: Path-integral Monte Carlo simulations of solid parahydrogen using two-body, three-body, and four-body ab initio interaction potential energy surfaces

Alexander Ibrahim<sup>1,2</sup> and Pierre-Nicholas Roy<sup>2, a)</sup>

<sup>1)</sup>Department of Physics and Astronomy, University of Waterloo, 200 University Avenue West, Waterloo, Ontario N2L 3G1, Canada

<sup>2)</sup>Department of Chemistry, University of Waterloo, 200 University Avenue West, Waterloo, Ontario N2L 3G1, Canada

## I. FIT PARAMETERS FOR THE MODIFIED BIRCH EOS

The average energy per particle as a function of density is fit to a modified Birch equation of state, given by

$$\epsilon = \epsilon_0 - \frac{P_0}{d\rho_0} + \frac{1}{\rho_0} \sum_{n=1}^4 \kappa_n d^{2n/3}, \quad (1)$$

where  $d = \rho/\rho_0$  and  $\rho_0 = 0.0261 \text{ \AA}^{-3}$ . We do this for the energy-density curves collected from simulations performed using both the S[2] and S[2, 3] sampling strategies, and using either of the E[2], E[2, 3], or E[2, 3, 4] estimations. In Tables (I) and (II), we show the fit parameters for the modified Birch EOS from simulations performed with the S[2] and S[2, 3] strategies, respectively. The fit parameters were found using `scipy.optimize.curve_fit()` with `scipy` version 1.14.1.

As a goodness-of-fit measure, we pick

$$\chi^2 = \frac{\sum_{i=1}^N w_i (\epsilon_i - \epsilon(\rho_i))^2}{\sum_{i=1}^N w_i}. \quad (2)$$

where  $w_i = 1/\sigma_i^2$  is the reciprocal of the standard error of the mean associated with the  $i$ th data sample,  $\epsilon_i$  is the mean of the  $i$ th data sample, and  $\epsilon(\rho_i)$  is the energy predicted by Eq. (1) at the  $i$ th density  $\rho_i$ . The value of  $\chi^2$  for each fit equation is given in the captions of Tables (I) and (II).

TABLE I. Parameters for Eq. (1), for the energy-density curves created from the E[2], E[2, 3], and E[2, 3, 4] estimates, collected from simulations using the S[2] sampling strategy. The parameter  $\epsilon_0$  is in unit of  $\text{cm}^{-1}$ , with the remaining five parameters in units of  $\text{cm}^{-1} \text{ \AA}^{-3}$ . The fits for the E[2], E[2, 3], and E[2, 3, 4] estimates have  $\chi^2$  values of 0.002832, 0.009615, and 0.001693, respectively.

	E[2]	E[2, 3]	E[2, 3, 4]
$\epsilon_0$	$-1.56505681 \times 10^3$	$-1.26250369 \times 10^2$	$3.56249208 \times 10^3$
$P_0$	$-3.75230222 \times 10^0$	$3.15494256 \times 10^0$	$1.51704339 \times 10^1$
$\kappa_1$	$1.02906387 \times 10^2$	$4.71395809 \times 10^1$	$-1.66626893 \times 10^2$
$\kappa_2$	$-1.09622970 \times 10^2$	$-8.40506135 \times 10^1$	$1.28837072 \times 10^2$
$\kappa_3$	$4.63227491 \times 10^1$	$5.07239623 \times 10^1$	$-5.28651108 \times 10^1$
$\kappa_4$	$-4.15077483 \times 10^0$	$-9.01830199 \times 10^0$	$1.12007899 \times 10^1$

<sup>a)</sup>Electronic mail: pnroy@uwaterloo.ca

TABLE II. Parameters for Eq. (1), for the energy-density curves created from the E[2], E[2, 3], and E[2, 3, 4] estimates, collected from simulations using the S[2, 3] sampling strategy. The units for the parameters match those given in the caption in Tab. (I). The fits for the E[2], E[2, 3], and E[2, 3, 4] estimates have  $\chi^2$  values of 0.002102, 0.008917, and 0.002962, respectively.

	E[2]	E[2, 3]	E[2, 3, 4]
$\epsilon_0$	$-1.83424519 \times 10^3$	$-5.49258462 \times 10^2$	$2.54277684 \times 10^3$
$P_0$	$-5.05459078 \times 10^0$	$1.04887723 \times 10^0$	$1.05389673 \times 10^1$
$\kappa_1$	$1.14397738 \times 10^2$	$6.47249178 \times 10^1$	$-1.20773904 \times 10^2$
$\kappa_2$	$-1.17679352 \times 10^2$	$-9.60762919 \times 10^1$	$9.44807408 \times 10^2$
$\kappa_3$	$4.88952562 \times 10^1$	$5.45899350 \times 10^1$	$-4.07315282 \times 10^1$
$\kappa_4$	$-4.43279955 \times 10^0$	$-9.51174267 \times 10^0$	$9.55183896 \times 10^0$

## II. ENERGY-DENSITY CURVES NEAR EQUILIBRIUM

In Fig. (1), we show the energy-density curves around the equilibrium density for the S[2] and S[2, 3] simulations.

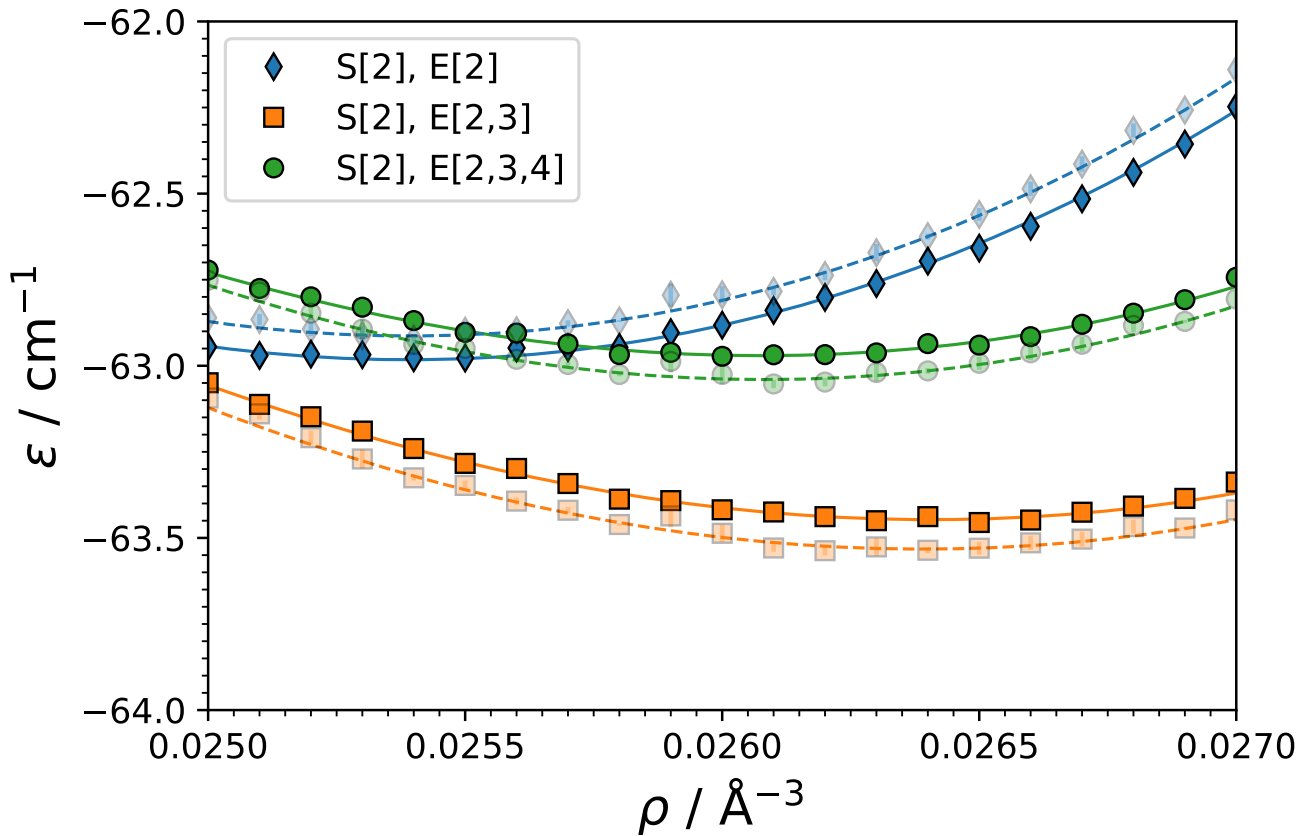


FIG. 1. The energy per molecule  $\epsilon$  as a function of the density  $\rho$  of solid parahydrogen around the equilibrium density for the E[2] (blue, diamonds), E[2, 3] (orange, squares), and E[2, 3, 4] (green, circles) estimates. Results from the S[2] simulations are shown with solid markers and solid lines, whereas results from the S[2, 3] simulations are shown with semitransparent markers and semitransparent dashed lines.

## III. ENERGY-DENSITY DATA

As part of the supplementary information, we have included the energy-density data used to create the equations of state in the manuscript. This includes the individual kinetic, two-body, three-body, and four-body interaction

energies per particle, as well as the two-body and three-body tail corrections.

The data is located within the submitted tarball. Also in the tarball is a `README.md` file with a more detailed description of the energy-density data.